Journal of Marine Science and Technology
DOI: 10.6119/JMST-013-0522-1

Determining the Internal Structure of Cement-based Materials by Using MRI Techniques

Hsiang-Wei Chiang[1], Ran Huang[1], and Chia-Jung Tsai[2]

Key words: pores, mortar, magnetic resonance imaging (MRI), mercury intrusion porosimetry (MIP)

ABSTRACT

The primary concerns of the internal structure of cement-based materials involve the distribution of pores, pore size, and the manner in which they are connected. Thoroughly understanding the distributive rules of pores and the approaches to breaking their links can contribute considerably to enhancing the durability of cement-based materials. Several methods are used to measure the pores of cement-based materials; however, they cannot determine the exact location of pores or structural links. Magnetic resonance imaging (MRI) has been widely applied in physical examinations and has matured to the level of being able to obtain 3D images of the organs of recipients without causing damage. In this study, MRI and mercury intrusion porosimetry (MIP) techniques were used to analyze the distribution of pores in mortar specimens with water-to-cement (w/c) ratios of 0.45, 0.55, and 0.65. The results indicate that MRI techniques can be used to determine the spatial distribution of pores and can obtain 3D images of pores in mortar.

I. INTRODUCTION

Cement-based material is a composite material that involves combining appropriate ratios of water, cement, aggregate, and admixtures to meet the various construction requirements of strength, durability, safety, workability, and economical efficiency. Because of construction factors, as well as physical and chemical factors, such as mixing and hydration, there are many pores in cement-based material. These pores were the focus of our research in studying the internal structure of cement-based material. Thoroughly understanding the distributive rules of pores and the approaches to breaking their links would contribute considerably to enhancing the durability of cement-based materials.

Current methods for measuring pores in cement-based materials include ultrasonic methods, microscopic observation using SEM, the rapid chloride permeability test used to assess the durability and capacity of cement-based material resistance to chloride ion intrusion, and mercury intrusion porosimetry (MIP) used to analyze the internal dimensions of pores [2,3]. Currently, MIP is acknowledged as an effective method for analyzing pores, and numerous scholars have adopted MIP. Using MIP facilitates obtaining data on three crucial properties of cement-based materials: the total cumulative volume of mercury intrusion, critical pore diameter, and pore size distribution (PSD). However, these methods cannot determine the precise location of pores or structural links. Currently, magnetic resonance imaging (MRI) can display the internal organs of the body in 3D images. MRI techniques have matured and numerous scholars have attempted to apply MRI in investigating cement-based materials [7,11,16]. Young et al. used MRI to measure cement paste. MRI was proven to be capable of spatially resolving crack structures with widths of tens of micrometers [20]. Jafer et al. also used MRI in research, and termed MRI a "complementary tool for imaging cement pastes" [15]. Jarny et al. used MRI to model the thixotropic behavior of fresh cement pastes [14]. Feng et al. also used MRI to examine Na and Li ion diffusion in a modified ASTM C 1260 test [9]. In this study, MRI is expected to be used for evaluating the distribution of pores in cement-based materials.

II. THEORY

The principles of MRI image acquisition are summarized as follows.

Specimens containing nuclei that can be magnetized are placed in a magnetic field with a magnetic field stronger than geomagnetism [4, 12]. Through the magnetic effect, the specimens are magnetized and produce a longitudinal magnetization vector. Subsequently, radiofrequency (RF) pulses are projected on the specimens. Magnetic nuclei within the specimens (for example, ^{1}H) resonate and produce a transverse magnetization vector. At this stage, spatial location coding is conducted con-

Paper submitted 11/28/12; revised 05/02/13; accepted 05/22/13. Author for correspondence: Ran Huang (e-mail: ranhuang1121@gmail.com).
[1]Department of Harbor and River Engineering, National Taiwan Ocean University, Keelung, Taiwan , R.O.C.
[2]Ph.D. Candidate, Institute of Materials Engineering, National Taiwan Ocean University, Keelung 202, Taiwan, R.O.C.

currently. The RF pulse can then be turned off to allow T1 relaxation and for T2 relaxation to occur in protons. T1 relaxation and T2 relaxation are collected via induction coils and transmitted to computers. Images can then be displayed by using 3D Fourier transformation.

The definition for T1 relaxation is as follows: the net magnetic moment (M_0) of hydrogen nuclei in the specimen as it turns to the XY plane after receiving 90° of RF energy; and the time required for the net magnetic moment to recover 63% of its original value after the RF is turned off, to allow the hydrogen nuclei to transmit the energy to the surrounding molecules. Therefore, the time required for longitudinal relaxation or for spin-lattice relaxation is called T1.

The definition of T2 relaxation is as follows: the net magnetic moment (M_0) of hydrogen nuclei as the specimen turns to the XY plane and becomes perpendicular (same phase) to the direction of RF after receiving 90°of RF energy; and the time required for the vector on the XY plane to decrease to 37% of its original value after the RF is turned off. Therefore, the time required for transverse relaxation or for pin-spin relaxation is called T2.

The T1 and T2 in porous materials are generally accepted to be related to the surface-to-volume ratio (S/V) of water-bearing pores as expressed by Equations (1) and (2) [13]

$$\frac{1}{T_1} = \rho_1 \frac{S}{V} \quad (1)$$

$$\frac{1}{T_2} = \rho_2 \frac{S}{V} \quad (2)$$

Here, the parameters ρ1 and ρ2 are the spin-lattice and spin-spin surface relaxivity constants. S and V are the surface area and volume of a pore respectively, which define the S/V ratio.

The signal magnitude at any point within a spin-echo image is given by Eq. (3).

$$S = \rho_0 e^{-\frac{t_p}{T_2^*}} \left(\frac{1 - e^{\frac{-TR}{T_1}}}{1 - \cos\alpha e^{\frac{-TR}{T_1}}} \right) \quad (3)$$

Here, ρo is the nuclei density, tp is the phase encoding time, TR is the repetition time, and α is the rotation angle for sample magnetization excited by a radio frequency (RF) pulse. T1 and T2* are the relaxation times of MRI.

Not every atom can be magnetized by the magnetism of a magnetic field to generate a longitudinal magnetization vector. When an atom has an odd number of electrons (not paired) and an odd number of protons, the spin is observable. Table 1 lists common magnetic nuclei.

The ^1H in H_2O was used as the source of MR imaging signals in this experiment to locate the distributed position of pores in mortar. ^1H was used because of its comparatively high gyromagnetic ratio, high sensitivity to magnetic fields, and easy access. Another reason for using ^1H was that the protons (hydrogen ions) found in solid calcium aluminate phases, hydroxyl (OH) groups of calcium hydroxide (CH), and calcium silicate hydrates (C–S–H) could not be identified because their T2, at 20 μs, was shorter than the detection limit [15]. Therefore, the mortar must be saturated before performing MRI, so that no other signals are generated in the mortar except for that of H_2O.

Additional theoretical details can be found in the following textbooks: *The Basics of MRI* and *Magnetic Resonance Imaging: Physical and Biological Principles*.

When a liquid does not wet a porous solid, it does not enter the pores in the solid through capillary action. The non-wetting liquid (mercury, in this test method) can be forced into the pores by applying external pressure. The sizes of the pores that are intruded are inversely proportional to the applied pressure. When a cylindrical pore model is assumed, the relationship between pressure and size is given as follows:

$$d = -4\gamma (\cos\theta) / P$$

where ＝the apparent pore diameter being intruded, γ＝the surface tension of the mercury, θ＝the contact angle between the mercury and the pore wall, and P＝the absolute pressure causing intrusion. Using this test method can obtain data on three crucial material properties: the total cumulative volume of mercury intrusion, critical pore diameter, and pore size distribution (PSD).

III. MATERIALS AND EXPERIMENTAL DETAILS

In previous applications, the common range of water-to-cement (w/c) ratios for cement-based materials with no admixture, such as fly ash, was between 0.40 and 0.60 [6]. The aim of this study was to investigate the distribution of pores in mortar at different w/c ratios. In this study, the w/c ratios of the mortar were set at 0.45, 0.55, and 0.65. River sand, cement, and water were mixed to produce mortars with w/c ratios of 0.45, 0.55, and 0.65, respectively. The percentage of mortar mixture in our tests was determined using the fixed sample volume method. The method is first used to determine water capacity. The cement is made according to the ratio of water to cement. The amount of sand can then be computed according to cement capacity. Hence, according to this method, the ratio of sand to cement is dynamic when the sample volume is fixed. Table 2 lists the proportions of the mortar mixture. Cylindrical mortar specimens with a dimension of 10 mm in diameter and approximately 22 mm in height were made for MRI. Cylindrical mortar specimens with a dimension of 18 mm in diameter and approximately 15 mm in height were made for MIP. Cube mortar specimens (51mm×51mm×51mm) were made for the compressive strength test. The mortars were then maintained in wet curing for 91 d and then air-dried for 48 h. Table 3 lists the specimen designations.

We used a 9.4 T (8.9 cm in diameter) upright superconducting MRI system. In this study, the vacuum method was used to obtain the saturation of mortar specimens, and the 25-mm diameter coil of the MRI system was used as the experimental coil [5, 19]. The software used in this study was the Para Vision 4.0 commercial image processing software.

The experimental process is described as follows:

Experiment 1:

Mortars A, B, and C, without any saturation treatment, were placed in the MRI system for scanning.

Experiment 2:

After **Experiment 1,** Mortars A, B, and C were infiltrated with water by using the vacuum method and were placed in the MRI system for scanning. Each mortar was scanned 3 times. Table 4 lists the established parameters of Experiments 1 and 2.

Experiment 3:

Cube mortar specimens with w/c ratios of 0.65, 0.55, and 0.45 were maintained in wet curing for 91 d. A compressive strength test method (ASTM C109 / C109M-11) was then conducted on these mortars [1].

Experiment 4:

In reference to ASTM D4404-10, MIP was conducted on Mortars D, E, and F.

IV. RESULTS AND DISCUSSION

We could not obtain any signals from Mortars A, B, or C without the mortars being saturated by the MRI system. The results indicated that mortars must undergo saturation treatment before MRI. Without performing this step, MRI systems cannot detect signals from the specimens.

Figs. 1a, 1b, 2a, 2b, 3a, and 3b illustrate the MRI scanning results for Mortars A, B, and C. Fig. 1a shows the vertical view of Mortar A. Fig. 1b shows one side of Mortar A. Figs. 2a and 2b are the images of Mortar B. Figs. 3a and 3b are the images of Mortar C.

After MRI scanning Mortars A, B, and C, the data from the MRI system were input into the Para Vision 4.0 software tool. Thus, we determined the required bright zones and applied the software tool to separate the required images from the unnecessary images.

The bright zones in an MRI image represent the signals obtained using the MRI system that originated from the H_2O in the pores of the mortars, with the number of bright zones corresponding with the number of pores. The location of water being the location of pores facilitated determining the spatial distribution of pores in the specimen.

Definition: The percentage of pores in mortars equals the volume of bright zones divided by the total volume of the mortar.

Here, the bright zone volume, which is acquired from the relationship between the voxel (pixel axis x × pixel axis y × pixel axis z) and resolution, refer to the colored sections in the MRI images. The total volume of the mortar was obtained using Archimedes's principle. The volume of the bright zones was then calculated. Table 5 lists the computation results from using Para Vision 4.0. The percentage of pores in Mortar A (0.038186±0.000943) exceeded that of Mortar B (0.032951±0.001068), and the percentage of pores in Mortar B exceeded that of Mortar C (0.028635±0.000394). Therefore, Mortar A had more pores than Mortar B did, and Mortar B had more pores than did Mortar C. Based on these results, we inferred that a higher w/c ratio implies a higher number of pores.

Table 6 presents the results of the compressive strength test of hydraulic mortars with w/c ratios of 0.65, 0.55, and 0.45. As shown in Table 8, the percentage of pores obtained from MRI (%) reduced to 86% of the value of 0.65 when the w/c ratio reduced to 0.55 from 0.65. Comparing the baseline w/c ratios equal to 0.65, for which the compressive strength values changed from 38.19 MPa to 43.68 MPa, revealed that the compressive strength increased 1.14 times. Similarly, the percentage of pores obtained from MRI (%) reduced to 74% of the value of 0.65 when the w/c ratio reduced to 0.45 from 0.65. Comparing the baseline w/c ratios equal to 0.65, for which the compressive strength values changed from 38.19 MPa to 55.14 MPa, revealed that the compressive strength increased 1.43 times. The MRI results suggest an inverse proportion of compressive strength and the percentage of pores. Thus, the results show that a higher w/c ratio indicates lower compressive strength, thereby leading to higher porosity, as indicated by the MRI results in Table 5 and the MIP results in Table 7.

Figs. 4, 5, and 6 show details of the relationship between the pore diameter and the cumulated amount of mercury intrusion, as derived from MIP experiments on Specimens D, E, and F.

Fig. 4 shows that, for Mortar D, the maximum mercury intrusion was 0.0071 mL/g, corresponding to a pore diameter of 95.3663 nm. The cumulative total of capillary porosity was 0.1034, and the total cumulative porosity was 0.1087, thus accounting for 95.11% of the porosity in the specimen.

Fig. 5 shows that, for Mortar E, the maximum mercury intrusion was 0.0053 mL/g, corresponding to a pore diameter of 68.3939 nm. The cumulative total capillary porosity was 0.0747, and the total cumulative porosity was 0.0790, thus accounting for 94.52% of the porosity in the specimen.

Fig. 6 shows that, for Mortar F, the maximum mercury intrusion was 0.0039 mL/g, corresponding to a pore diameter of 68.4792 nm. The cumulative total capillary porosity was 0.0663, and the total cumulative porosity was 0.0724, thus accounting for 91.64% of the porosity in the specimen.

However, MIP exhibits defects [8, 10, 16, 18]. In MIP, pores are assumed to be cylindrical, but they are actually not. The pressurizing process may damage the pore wall of relatively thin pores and result in new channels. In addition, "ink-bottles" may appear in specimens, potentially affecting experimental results by causing an overestimation of the amount of mercury (Hg) penetration in smaller pores and an underestimation of the amount of Hg penetration in larger pores. Therefore, results obtained using MIP might deviate from actual conditions. With or without errors, such as the ink-bottles in the MIP experiment, the total volume of Hg poured into the specimens equaled the total volume of pores in the specimen. In the MRI experiment, the total volume of bright zones represented the volume of pores in the specimen. Because different specimens were used in the MIP and MRI experiments, we compared the percentage values of the pores from the MIP and MRI experiments. Table 5 lists the values of the total bright zones and the total volume of the specimens obtained using MRI, and the total amount of poured Hg that contained different w/c ratios are listed in Table 7. Table 8 presents the results of MRI, as compared with those from MIP and strength experiments.

When w/c = 0.65, the percentage of pores obtained in the MRI experiment was 19.81 % of that obtained in the MIP experiment. When w/c = 0.55, the percentage of pores obtained in the MRI experiment was 20.50 % of that obtained in the MIP experiment. When w/c = 0.45, the percentage of pores obtained in the MRI experiment was 18.49% of that obtained in the MIP experiment. The results indicate that the MRI experiment could

be used to determine the spatial distribution of the pores in the specimen.

Regardless of the mortar's w/c ratio, the MRI experiment can at least achieve approximately 18.5% of the mortar's total pore volume. Currently, we are experiencing difficulties in processing the mortar after MIP and extracting Hg from the mortar. Furthermore, Hg is neurologically toxic and must be used with caution. To avoid influences of the MIP experiment on the environment, the proportional relationship between MRI and MIP experiments should be used, and the MRI experiment should be conducted to determine the mortar's pore volume.

V. CONCLUSION

The MRI technique successfully imaged water held in the pores of a saturation treatment mortar. Mortar must undergo saturation treatment prior to MRI experiments. Otherwise, signals cannot be detected. In contrast to Young's MRI study on the surface crack of mortar specimens, the results of our experiment yielded the internal pore images of cement-based materials. The results of the MRI experiment demonstrated that a higher w/c implies a higher volume ratio of bright zones. In addition, because the signals of bright zones obtained using the MRI system originated from the H_2O in the pores of the mortars, the number of bright zones corresponds with the number of pores. The MRI results revealed that a higher w/c implies a higher volume ratio of bright zones; thus, a higher w/c indicates a higher number of pores. These results were further compared to the results from the compressive strength test of hydraulic mortars, thus indicating that a higher w/c correlates with lower compressive strength.

In the MIP experiment, the volume of poured Hg represented the volume of pores in the specimen. In the MRI experiment, the volume of bright zones represented the volume of pores in the specimen. Assuming that the results obtained from the MIP experiment are correct, by comparing the percentage value of pores from different specimens obtained from the MIP and MRI experiments, the results show that the average percentage value of pores obtained in the MRI experiment was 19.28% of that for the MIP experiment. Therefore, by reversely estimating the percentage value of pores from the MRI experiment (19.28%), that for the MIP experiment can be inferred; thus, the pore volume of the entire cement-based materials can also be estimated. The MIP experiment is time consuming. Thus, to prevent the negative influence on the environment caused by Hg, the MIP experiment might be replaced by that of the MRI to estimate the pore volume in cement-based materials. Furthermore, based on previous studies, the size of gel pores is approximately 0.5–10 nm [21], which exceeds the resolution range of current MRIs. Therefore, only the spatial distribution of large pores, such as capillary pores and compaction pores in mortar, can be acquired using MRI.

ACKNOWLEDGMENTS

The authors wish to express their appreciation to the Preparatory Office of the Institute of Biomedical Sciences (IBMS) for providing the venue and MRI system required for this experiment.

REFERENCES

1.*ASTM C109 / C109M – 11, Standard Test Method for Compressive Strength of Hydraulic Cement Mortars (Using 2-in. or [50-mm] Cube Specimens*, American Society of Testing and Materials (ASTM), ASTM International, USA (2011).

2.*ASTM C1202-97, Standard test method for electrical indication of concrete's ability to resist chloride ion penetration*, American Society of Testing and Materials (ASTM), ASTM International, USA (1997).

3.*ASTM D 4404 –10, Standard Test Method for Determination of Pore Volume and Pore Volume Distribution of Soil and Rock by Mercury Intrusion Porosimetry*, American Society of Testing and Materials (ASTM), ASTM International, USA (2010).

4.Bushong, S. C., *Magnetic resonance imaging: Physical and biological principles*, 2nd ed., Mosby-Year Book (1996).

5.Chiang, C.-T., *Activation Energy of Electrical Conductivity by the Rapid Chloride Permeability Test of Concrete*, Ph.D. Dissertation, Materials Engineering College of Engineering National Taiwan Ocean University, Keelung, Taiwan, Republic of China (2009).

6.Chinese institute of civil and hydraulic engineering, *Concrete: Scientific & Technical*, Chinese institute of civil and hydraulic engineering Publishing Co., Ltd (2011).

7.Chou, M. C., Tsai, P. H., Huang, G. S., Lee, H. S., Lee, C. H., Lin, M. H., Lin, C.-Y., and Chung, H. W., "Correlation between the MR T2 value at 4.7 T and relative water content in articular cartilage in experimental osteoarthritis induced by ACL transaction," *Osteoarthritis Cartilage*, Vol. 17, No. 4, pp. 441-447 (2009).

8.Cook, R. A. and Hover, K. C., "Mercury porosimetry of hardened cement pastes," *Cement Concrete Res*, Vol. 29, pp. 933-943 (1999).

9.Feng, X., Balcom, B. J., Thomas, M. D. A., and Bremner, T. W., "Na and Li ion diffusion in modified ASTM C 1260 test by Magnetic Resonance Imaging (MRI)," *Cement and Concrete Research*, Vol. 38, No. 12, pp. 1409-1415 (2008).

10.Galle, C., "Effect of drying on cement-based materials pore structure as identified by mercury intrusion porosimetry - A comparative study between oven-, vacuum-, and freeze-drying," *Cement and Concrete Research*, Vol. 31, pp. 1467-1477 (2001).

11.Hornak, J. P., "The Basics of MRI," Retrieved from http://www.cis.rit.edu/htbooks/mri/

12.Huang, G. S., Lee, H. S., Chou, M. C., Shih, Y. Y., Tsai, P. H., Lin, M. H., Lin, C.-Y., Lee, C. H., and Chung, H. W., "Quantitative MR T2 measurement of articular cartilage to assess the treatment effect of intra-articular hyaluronic acid injection on experimental osteoarthritis induced by ACLX," *Osteoarthritis Cartilage*, Vol. 18, pp. 54-60 (2008).

13.Jaffer, S. J., Lemaire, C., Hansson, C. M., and Peemoeller, H., "MRI: A complementary tool for imaging cement pastes," *Cement and Concrete Research*, Vol. 37, pp. 369-377 (2007).

14.Jarny, S., Roussel, N., Le Roy, R., and Coussot, P., "Modelling thixotropic behavior of fresh cement pastes from MRI measurements," *Cement and Concrete Research*, Vol. 38, No. 5, pp. 616-623 (2008).

15.Kleinberg, R. L., Kenyon, W. E., and Mitra, P. P., "Mechanism of nmr relaxation of fluids in rock," *Journal of Magnetic Resonance, Series A*, Vol. 108, pp. 206-214 (1994).

16.Konecny, L. and Naqvi, S. J., "The effect of different drying techniques on the pore size distribution of blended cement mortars," *Cement and Concrete Research*, Vol. 23, pp. 1223-1228 (1993).

17.Lin, C.-Y., Lin, M.-H., Cheung, W.-M., Lin, T.-N., Chen, J.-H., and Chang, C., "In Vivo Neuro-microvasculatural Visualization using 3D ΔR2-Based Microscopy of Magnetic Resonance Angiography (3DΔR2-mMRA)," NeuroImage,, Vol. 45, No. 3, pp. 824-831 (2009).

18.Ramachandran, V. S. and Beaudoin, J. J., *Handbook of analytical techniques in concrete science and technology: Principles, techniques and application*, Noyes Publications / William Andrew Publishing, LLC, Norwich, New York (2001).

19.Safiuddin, Md. and Hearn, N., "Comparison of ASTM saturation techniques for measuring the permeable porosity of concrete," *Cement and Concrete Research*, Vol. 35, pp. 1008-1013 (2005).

20.Young, J. F. and Mindness, S., *The Science and Technology of Civil Engineering Materials*, Prentice Hall (1998).

21.Young, J. J., Szomolanyi, P., Bremner, T. W., and Balcom, B. J., "Magnetic resonance imaging of crack formation in hydrated cement paste materials," *Cement and Concrete Research*, Vol. 34, pp. 1459-1466 (2004).

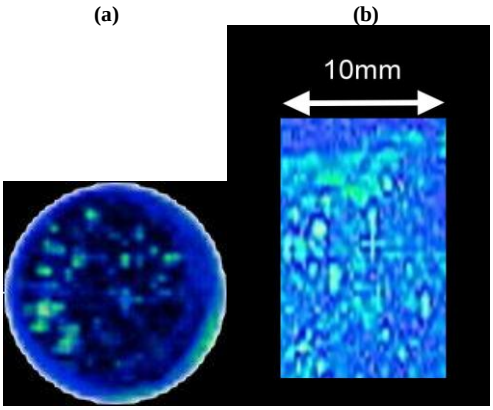

Fig. 1. (a) and (b)illustrate the MRI results for Mortar A (w/c = 0.65).

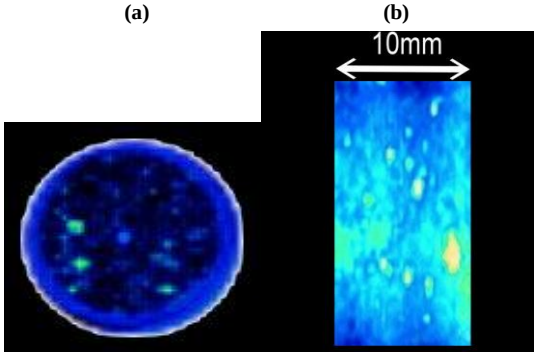

Fig. 2. (a) and (b) illustrate the MRI results for Mortar B (w/c = 0.55).

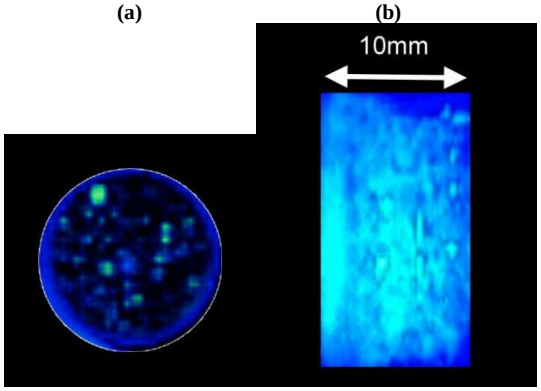

Fig. 3. (a) and (b) illustrate the MRI results for Mortar C (w/c = 0.45).

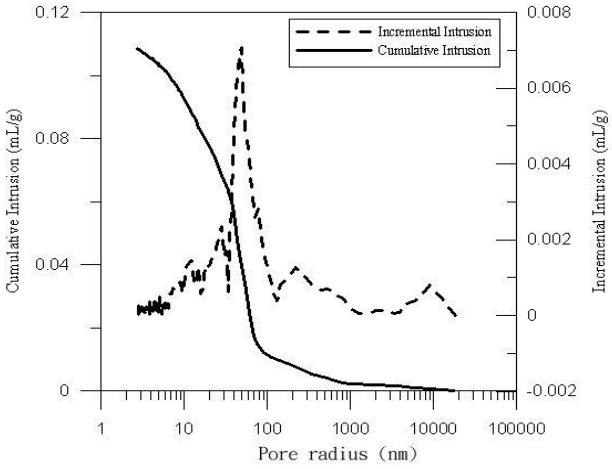

Fig. 4. Relationship between pore diameter and mercury intrusion (W/C=0.65).

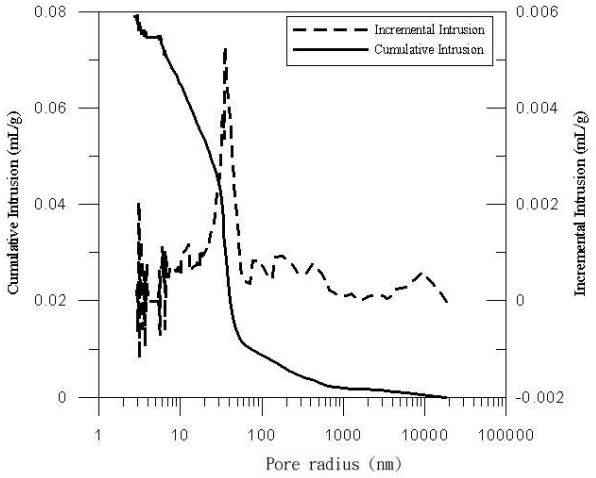

Fig. 5. Relationship between pore diameter and mercury intrusion (W/C=0.55).

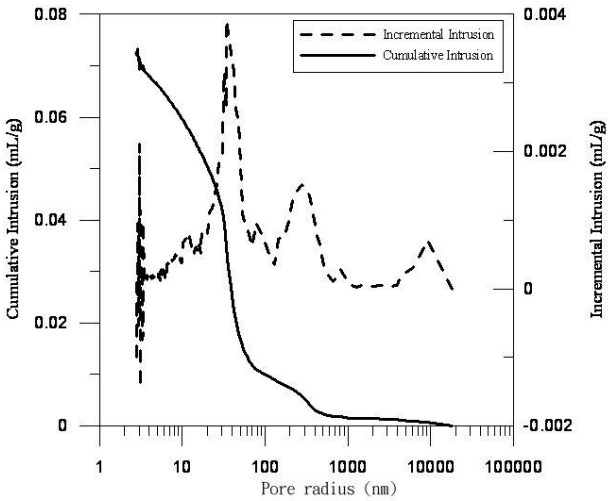

Fig. 6. Relationship between pore diameter and mercury intrusion (W/C=0

Table 1. Common magnetic nuclei and their relative magnetic susceptibility.

Common magnetic nuclei	Relative magnetic susceptibility
^{1}H	1.0
^{14}N	0.083
^{31}P	0.066
^{13}C	0.016
^{23}Na	0.093
^{29}K	0.0005
^{19}F	0.83

Table2. Mix design of the mortars.

w/c / Item	0.65	0.55	0.45
Water (g)	335	329	321
Cement (g)	516	599	714
River sand (g)	1185	1134	1064

Table 3. Specimen designation.

Specimen	w/c ratio	Treatment
A	0.65	MRI experiment
B	0.55	MRI experiment
C	0.45	MRI experiment
D	0.65	ASTM D 4404 –10
E	0.55	ASTM D 4404 –10
F	0.45	ASTM D 4404 –10
65Cube1	0.65	ASTM C109 / C109M-11
65Cube2	0.65	ASTM C109 / C109M-11
65Cube3	0.65	ASTM C109 / C109M-11
55Cube1	0.55	ASTM C109 / C109M-11
55Cube2	0.55	ASTM C109 / C109M-11
55Cube3	0.55	ASTM C109 / C109M-11
45Cube1	0.45	ASTM C109 / C109M-11
45Cube2	0.45	ASTM C109 / C109M-11
45Cube3	0.45	ASTM C109 / C109M-11

Table4. Established parameters of the MRI system.

Specimen / Established parameter	Saturated processing	TR	TE	FOV	NEX	Matrix size	Reso-lution	Scan time
Mortar A Mortar B Mortar C	× × ×	10 ms	0.036 ms	3.0*3.0* 4.0 cm	8	128*64 *64 → (interpol -ate to) 256*128 *128	117 *235 * 316 μm	11hr, 39min
First time to scan Mortar A	○ vacuum method	10 ms	0.026 ms	5.0*5.0* 5.0 cm	1	128*128 * 128	391 *391 * 391 μm	5hr, 49min
Second time to scan Mortar A	○ vacuum method	10 ms	0.026 ms	5.0*5.0* 5.0 cm	1	128*128 * 128	391 *391 * 391 μm	5hr, 49min
Third time to scan Mortar A	○ vacuum method	10 ms	0.026 ms	5.0*5.0* 5.0 cm	1	128*128 * 128	391 *391 * 391 μm	5hr, 49min
First time to scan Mortar B	○ vacuum method	10 ms	0.026 ms	5.0*5.0* 5.0 cm	1	128*128 * 128	391 *391 * 391 μm	5hr, 49min
Second time to scanMortar B	○ vacuum method	10 ms	0.026 ms	5.0*5.0* 5.0 cm	1	128*128 * 128	391 *391 * 391 μm	5hr, 49min
Third time to scan Mortar B	○ vacuum method	10 ms	0.026 ms	5.0*5.0* 5.0 cm	1	128*128 * 128	391 *391 * 391 μm	5hr, 49min
First time to scan Mortar C	○ vacuum method	10 ms	0.026 ms	5.0*5.0* 5.0 cm	1	128*128 * 128	391 *391 * 391 μm	5hr, 49min
Second time to scan Mortar C	○ vacuum method	10 ms	0.026 ms	5.0*5.0* 5.0 cm	1	128*128 * 128	391 *391 * 391 μm	5hr, 49min
Third time to scan Mortar C	○ vacuum method	10 ms	0.026 ms	5.0*5.0* 5.0 cm	1	128*128 * 128	391 *391 * 391 μm	5hr, 49min

Table5. Results of MRI experiment.

Result / Specimen	Volume of the specimen (cm^3)	Volume of bright zones obtained using MRI (cm^3)	Average of the volume of bright zones obtained using MRI (cm^3)	Standard deviation	Volume of bright zones / volume of the specimen
First time to scan Mortar A	1.7269	0.064526	0.065944	0.00163	0.038186 ± 0.000943
Second time to scan Mortar A		0.067726			
Third time to scan Mortar A		0.065581			
First time to scan Mortar B	1.7271	0.056442	0.056910	0.001845	0.032951± 0.001068
Second time to scan Mortar B		0.058943			
Third time to scan Mortar B		0.055344			
First time to scan Mortar C	1.7278	0.048695	0.049475	0.00682	0.028635± 0.000394
Second time to scan Mortar C		0.049958			
Third time to scan Mortar C		0.049773			

Table 6. Compressive strength of mortars.

Item / w/c	Specimen	Compressive strength（MPa）	Average（MPa）
0.65	65Cube1	38.43	38.19
	65Cube2	38.09	
	65Cube3	38.05	
0.55	55Cube1	46.95	43.68
	55Cube2	44.46	
	55Cube3	39.64	
0.45	45Cube1	54.78	55.14
	45Cube2	57.27	
	45Cube3	53.35	

Table 7. Results of MIP experiment.

Specimen / Obtain data from MIP	Mortar D w/c:0.65	Mortar E w/c:0.55	Mortar F w/c:0.45
Maximum mercury intrusion(mL/g)	0.0071	0.0053	0.0039
Maximum mercury intrusion corresponding to pore diameter (nm)	95.3663	68.3939	68.4792
Cumulative total of capillary porosity (mL/g)	0.1034	0.0747	0.0663
Total cumulative porosity(mL/g)	0.1087	0.0790	0.0724
Cumulative total of capillary porosty/total cumulative porosity (%)	95.11	94.52	91.64
Weight of specimen(g)	7.1528	7.9958	7.7454
Volume of Mercury Intrusion(cm^3)	0.7397	0.6318	0.5604
Volume of specimen(cm^3)	3.8363	3.9243	3.6214
Total volume of mercury intrusion/ volume of specimen(%)	19.28	16.10	15.47

Table 8. Comparisons of MRI experiment results with those of and the MIP experiment and strength test.

Data from different experiment / w/c	Compressive strength (MPa)	Percentage of pores obtained from MRI (%) (total bright zones/total volume of the specimen)	Percentage of pores obtained from MIP (%) (Total volume of pores obtained using MIP/ the total volume of the specimen)	Percentage of pores obtained from MRI/ percentage of pores obtained from MIP (%)
0.65	38.19	3.82	19.28	19.81
0.55	43.68	3.30	16.10	20.50
0.45	55.14	2.86	15.47	18.49